

# Time Domain Simulations using the Modified Myers Boundary Condition

Edward J. Brambley\*

*DAMTP, University of Cambridge, UK*

and

Gwénaél Gabard†

*ISVR, University of Southampton, UK*

This paper considers the simplistic 2D problem of a time-harmonic point/line mass source in uniform flow over an acoustic lining in order to investigate the relationship between time-domain numerical instabilities and “real” instabilities of flow over acoustic linings. An exact analytic solution is given for the long-time time-harmonic solution to this problem, and this is compared with a numerical time-domain solution which is carefully constructed so as not to need any selective filtering. A discrete dispersion analysis is then performed to analyse the temporal stability of this entire numerical scheme when subjected to impedance boundary conditions.

The numerical instability commonly present in time-domain simulations using the Myers boundary condition is indeed shown to correspond to the illposedness of the underlying mathematical model, as previously predicted. Moreover, the modified boundary condition proposed by Brambley is numerically implemented and the stability of this boundary condition is analysed. The modified boundary condition is shown to lead to a separation in wavenumber between “real” instabilities of the underlying problem and spurious numerical instabilities, which should enable future implementations to remove the numerical instabilities while retaining any “real” instabilities.

The analytic benchmark solution developed here may prove useful for numerical validation purposes, especially with regard to stability and instability.

## I. Introduction

Acoustic linings and the effects of their presence, position, and properties continue to be of major importance to sound reduction in aeroengines. However, the mathematical modelling of acoustic linings and the implementation of that modelling in frequency- or time-domain numerical simulations is still not fully resolved. For instance, the question of whether flow over acoustic linings can in some circumstances be unstable continues to be debated<sup>1–8</sup>, with mathematical theory, numerical simulations and experimental observations not agreeing with one another.

The boundary condition often used in numerical simulations involving flow over acoustic linings is the Myers<sup>9</sup>, or Ingard–Myers<sup>10</sup>, boundary condition. This boundary condition correctly represents the limit of a vanishingly-thin inviscid boundary layer over the acoustic lining<sup>11,12</sup>, although the boundary layer needs to be extremely thin in some cases for this to be a good approximation<sup>13</sup>. In time-domain simulations this boundary condition is known to lead to numerical instabilities, believed to be spurious and therefore filtered out using an artificial selective filter<sup>14–18</sup>. The unfortunate consequence of this is that, by definition,

---

\*Royal Society University Research Fellow, Department of Applied Mathematics & Theoretical Physics, University of Cambridge, CMS, Wilberforce Road, Cambridge CB3 0WA, United Kingdom. AIAA member.

†Lecturer, Institute of Sound and Vibration Research, University of Southampton, Highfield, Southampton, SO17 1BJ, United Kingdom. AIAA senior member.

Copyright © 2013 by E. J. Brambley & G. Gabard. Published by the American Institute of Aeronautics and Astronautics, Inc. with permission.

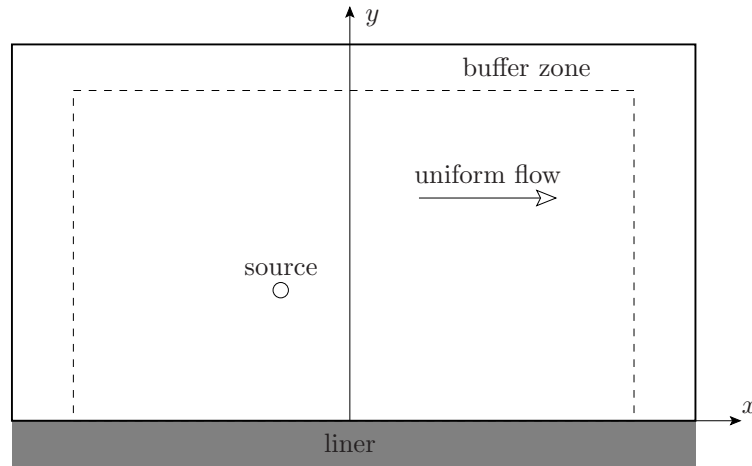


Figure 1. Diagram of the benchmark problem.

such simulations always predict the flow over acoustic linings to be stable, which may not reflect reality<sup>6</sup>. Brambley<sup>4</sup> suggested the root cause of this numerical instability is that the underlying mathematical problem is illposed, which is also the reason why a rigorous stability analysis is not possible; hence the continuing debate over stability. Recently, Rienstra and Darau<sup>7</sup> and Brambley<sup>5</sup> independently suggested modifications to the Myers boundary condition to overcome this illposedness, although subsequent results suggest that the modification of Rienstra and Darau<sup>7</sup> can cause some unwanted side effects<sup>19</sup>. However, to date, there has been no conclusive proof that the illposedness highlighted by Brambley<sup>4</sup> is indeed the root cause of the time-domain numerical instability, nor has there been a demonstration that any suggested modification to the Myers boundary condition can be successfully implemented in the time domain. This paper aims to address the first of these, and to make a start on the second.

## II. Problem description

As a simple situation on which to analyse the behaviour of flow over acoustic linings, we consider the two-dimensional problem, shown in figure 1, of a uniform mean flow in the  $x$  direction of constant velocity  $u_0$ , constant sound speed  $c_0$  and constant density  $\rho_0$ . The propagation of linear disturbances on this uniform mean flow is described by the linearized Euler equations (LEE), which may be written as

$$\frac{\partial \mathbf{q}}{\partial t} + \mathbf{F}_x \frac{\partial \mathbf{q}}{\partial x} + \mathbf{F}_y \frac{\partial \mathbf{q}}{\partial y} = \mathbf{s}, \quad (1)$$

where

$$\mathbf{q} = \begin{bmatrix} \rho' \\ (\rho u)' \\ (\rho v)' \\ p' \end{bmatrix}, \quad \mathbf{F}_x = \begin{bmatrix} 0 & 1 & 0 & 0 \\ -u_0^2 & 2u_0 & 0 & 1 \\ -u_0 v_0 & v_0 & u_0 & 0 \\ -u_0 c_0^2 & c_0^2 & 0 & u_0 \end{bmatrix}, \quad \mathbf{F}_y = \begin{bmatrix} 0 & 0 & 1 & 0 \\ -u_0 v_0 & v_0 & u_0 & 0 \\ -v_0^2 & 0 & 2v_0 & 1 \\ -v_0 c_0^2 & 0 & c_0^2 & v_0 \end{bmatrix}.$$

The source  $\mathbf{s}$  we consider here is a time-harmonic acoustic point monopole with angular frequency  $\omega$  located at  $(x_s, y_s)$ , defined by

$$\mathbf{s} = \begin{bmatrix} 1 \\ u_0 \\ v_0 \\ c_0^2 \end{bmatrix} \delta(x - x_s) \delta(y - y_s) \sin(\omega t). \quad (2)$$

The acoustic waves radiating from the source interact with a lined surface located along  $y = 0$ . This lining is characterized by its acoustic impedance  $\hat{Z}(\omega)$  given in the frequency domain (with an  $\exp(+i\omega t)$  notation). The interaction between the liner and the sound field may be described using the Myers boundary condition<sup>9</sup>,

$$i\omega \hat{v}_n(x, \omega) = \left( i\omega + u_0 \frac{\partial}{\partial x} \right) \frac{\hat{p}(x, 0, \omega)}{\hat{Z}(\omega)}, \quad (3)$$

where  $\hat{v}_n = -\hat{v}(x, 0, \omega)$  is the normal velocity into the surface. This condition assumes an infinitely thin boundary layer, and effectively uses a vortex sheet model where the continuity of pressure and normal displacement is applied<sup>11–13</sup>. Taking account of a finite thickness inviscid boundary layer leads to a modified Myers boundary condition, and here we follow the modification due to Brambley<sup>5</sup>. If we consider a single Fourier component  $e^{+i\omega t - ikx}$ , then this boundary condition reads (equation (9) in Ref. 5 with  $U(1) = 0$ )

$$\left[ i\omega\hat{Z} + \rho_0(\omega - u_0k)^2\delta I_0(\omega, k) \right] \hat{v}_n = \left[ i(\omega - u_0k) - \frac{\omega\hat{Z}\delta I_1(\omega, k)k^2}{\rho_0(\omega - u_0k)} \right] \hat{p}. \quad (4)$$

Here, we will assume a linear-then-constant velocity profile and a uniform density profile for the boundary layer, for which

$$(\omega - u_0k)^2\delta I_0 = -\omega k u_0 \delta + \frac{2}{3}k^2 u_0^2 \delta, \quad \delta I_1 = \delta u_0 k / \omega, \quad (5)$$

where  $\delta$  is the boundary layer thickness.

A number of models for the impedance  $\hat{Z}(\omega)$  may be used. Here, due to its ease of numerical implementation, we adopt a mass–spring–damper impedance

$$\hat{Z}(\omega) = R + im\omega - iK/\omega = 2m\omega_0 d + im(\omega - \omega_0^2/\omega), \quad (6)$$

where  $m$ ,  $K$  and  $R$  are the mass, spring stiffness and damping coefficients (per unit length) of the resonator,  $\omega_0 = \sqrt{K/m}$  is the undamped resonance frequency and  $d = R/(2m\omega_0)$  is the damping coefficient. Other popular impedance models include the Extended Helmholtz Resonator<sup>20</sup> and the three parameter model<sup>14</sup>, which differ in the way they are formulated and implemented in the time domain, as well as in their ability to represent realistic impedance functions. It should be emphasized that the interest of this paper is in investigating the behaviour of the boundary conditions (3) and (4), and not in the specific impedance model (6) used. It is anticipated that what follows will be similarly applicable to other models of the impedance.

### III. Numerical model

The field equations (1) are solved in the time domain using finite difference schemes on a rectangular computational domain defined by  $-L < x < L$  and  $0 < y < H$ . The grid uses  $N_x$  and  $N_y$  grid points in the  $x$  and  $y$  directions. Spatial derivatives are approximated using the 7-point DRP stencils of Tam and Webb<sup>21</sup> and Berland et al.<sup>22</sup> optimized for low dispersion. An optimized 6-stage Runge–Kutta scheme is used for time marching<sup>23</sup>. A 7-point selective filter<sup>23</sup> may be applied at each time step to remove the spurious short-wavelength components that are sometimes supported by low-dispersion low-dissipation schemes. However, it will be seen later that due to the choice of this numerical scheme and discretization, such selective filtering is not necessary, and is included here only to demonstrate the effects of such filtering.

Within the numerical model, the point monopole source term (2) is modified to a Gaussian monopole of width  $w$ , defined by

$$\mathbf{s} = \begin{bmatrix} 1 \\ u_0 \\ v_0 \\ c_0^2 \end{bmatrix} \exp \left[ -\frac{(x - x_s)^2 + (y - y_s)^2}{2w^2} \right] \frac{\sin(\omega t)}{\sqrt{2\pi w^2}}.$$

Typically, the width  $w$  will be only a few grid points, so that the Gaussian monopole is a good approximation to a point monopole.

#### A. Myers boundary condition

To implement the mass–spring–damper impedance boundary (6) using the Myers boundary condition (3) in the time domain, one has to deal with the term  $\hat{p}(\omega)/\hat{Z}(\omega)$  which, when written in the time domain, represents a convolution between the acoustic pressure at the surface and an impulse response function for the liner. This must be done in such a way that a number of basic physical principles, including causality, are satisfied<sup>20</sup>. To that end we introduce an auxiliary variable  $\eta$  such that:

$$\hat{\eta}(x, \omega) = \hat{p}(x, 0, \omega)/\hat{Z}(\omega).$$

The mass–spring–damper model defined by (6) can then be implemented with the following coupled equations:

$$\frac{\partial \eta(x, t)}{\partial t} = \frac{1}{m} [p'(x, 0, t) - K\xi(x, t) - R\eta(x, t)] , \quad \frac{\partial \xi(x, t)}{\partial t} = \eta(x, t) , \quad (7)$$

This implementation of the impedance satisfies all the conditions given in Ref. 20. The auxiliary variable  $\xi$  corresponds to the displacement of the mass–spring–damper, which is also the displacement of the fluid for this boundary condition. The variable  $\eta$  corresponds to the normal velocity between the vortex sheet and the liner, in contrast to the normal velocity  $v_n$  which is defined above the vortex sheet. The Myers boundary condition (3), written in the time domain, relates the two normal velocities  $\eta$  and  $v_n$  on either sides of the vortex sheet:

$$\frac{\partial v_n(x, t)}{\partial t} = \frac{\partial \eta(x, t)}{\partial t} + u_0 \frac{\partial \eta(x, t)}{\partial x} . \quad (8)$$

The second term on the right-hand side is often called the convective term. The time derivative of  $\eta$  is provided directly by (7), and the spatial derivative of  $\eta$  is calculated using the same finite-difference stencils as for the LEE. Equation (7) is easily implemented by defining the two auxiliary variables  $\eta$  and  $\xi$  at each grid point on the impedance boundary. These variables are integrated in time using (7) and the local value of pressure. The same time-marching scheme as for the LEE is used. An important note is that all these book-keeping calculations are purely local, since they do not require information from neighbouring grid points, which significantly simplifies the implementation of this boundary, especially if a parallelized multi-block grid method is used.

Equation (8) is used to modify the field equations (1) solved along the impedance surface  $y = 0$ . A straightforward approach would be to substitute the third equation in (1) by

$$\frac{\partial(\rho v)'}{\partial t} = -\rho_0 \frac{\partial \eta(x, t)}{\partial t} - \rho_0 u_0 \frac{\partial \eta(x, t)}{\partial x} , \quad \text{at } y = 0 . \quad (9)$$

However, we found that this approach leads to unnecessary numerical instabilities even for a rigid wall for which  $\eta \equiv 0$ . Instead, we use the characteristics of the governing equations (1), and modify the incoming characteristic in such a way that the boundary condition (8) is satisfied, as described by Higdon<sup>24</sup> and Kim and Lee<sup>25</sup>. As will be seen, this results in a stable simulation for a rigid wall even without numerical selective filtering.

## B. Modified Myers boundary condition

The modified Myers boundary condition implemented here is given in (4), with  $\delta I_0$  and  $\delta I_1$  given by (5). However, the last term of equation (4) is not in a form that is convenient for numerical implementation. We use the momentum equation

$$i\rho_0(\omega - ku_0)\hat{u} - ik\hat{p} = 0 ,$$

to rewrite this term using the tangential velocity  $\hat{u}$ . The boundary condition becomes

$$i\omega \hat{v}_n(x, \omega) = \left( i\omega + u_0 \frac{\partial}{\partial x} \right) \frac{\hat{p}(x, 0, \omega)}{\hat{Z}(\omega)} + \delta u_0 \left\{ \frac{\partial^2 \hat{u}(x, 0, \omega)}{\partial x^2} + \rho_0 \left( \frac{\partial^2}{\partial t \partial x} + \frac{2}{3} u_0 \frac{\partial^2}{\partial x^2} \right) \frac{\hat{v}_n(x, 0, \omega)}{\hat{Z}(\omega)} \right\} . \quad (10)$$

For the first term on the right-hand side we introduce the same auxiliary variables  $\eta$  and  $\xi$  as defined by (7). In addition, we also introduce two other auxiliary variables  $\tilde{\eta}$  and  $\tilde{\xi}$  in order to implement the term  $\hat{v}_n(x, 0, \omega)/\hat{Z}(\omega)$  in the time domain. These variables follow similar definitions to  $\eta$  and  $\xi$ :

$$\frac{\partial \tilde{\eta}(x, t)}{\partial t} = \frac{1}{m} [v_n(x, 0, t) - K\tilde{\xi}(x, t) - R\tilde{\eta}(x, t)] , \quad \frac{\partial \tilde{\xi}(x, t)}{\partial t} = \tilde{\eta}(x, t) . \quad (11)$$

In the time domain, equation (10) becomes

$$\frac{\partial v_n(x, t)}{\partial t} = \frac{\partial \eta(x, t)}{\partial t} + u_0 \frac{\partial \eta(x, t)}{\partial x} + \delta u_0 \left\{ \frac{\partial^2 u(x, 0, t)}{\partial x^2} + \rho_0 \left[ \frac{\partial}{\partial x} \frac{\partial \tilde{\eta}(x, t)}{\partial t} + \frac{2}{3} u_0 \frac{\partial^2 \tilde{\eta}(x, t)}{\partial x^2} \right] \right\} .$$

The terms  $\partial \eta / \partial t$  and  $\partial \tilde{\eta} / \partial t$  are directly given by (7) and (11). The spatial derivatives are calculated using the same finite-difference stencils as for the LEE. This is easily implemented by defining the four auxiliary variables at each grid point on the impedance boundary, as for the unmodified Myers boundary condition, and in the same way, the calculations in (7) and (11) are all local and so do not require information from neighbouring grid points.

### C. Buffer zones

To simulate an infinite domain, buffer zones are implemented at the upper and lateral boundaries using a method similar to that of Karni<sup>26</sup> and Sandberg and Sandham<sup>27</sup>. At each time step, the amplitudes of the incoming characteristics along the direction normal to the boundary are progressively scaled down while the outgoing characteristics are left unchanged throughout the buffer zone.

## IV. Analytic solution

In order to verify the results of our numerical simulations with theoretical predictions, an analytic model is developed to find the long-time time-harmonic solution to (1) subject to the time-harmonic monopole point-forcing (2). Despite the simplicity of this situation, what follows appears to be new: Morse and Ingard<sup>28</sup> do not seem to include the solution (even without mean flow); Junger and Feit<sup>29</sup>, p. 371 state that an analytic solution is not available in closed form for the no-flow case; and Ju and Fung<sup>30</sup> do not consider the issue of the causal, unstable solution.

In this section only, we nondimensionalize so that  $c_0 = 1$ ,  $\rho_0 = 1$ , and  $u_0 = M$  is the Mach number of the flow. Without loss of generality, we also set the  $x$ -origin such that  $x_s = 0$ . Rearranging in terms of the perturbation pressure  $p'$  and considering first the Myers boundary condition given by (3), the problem to be solved is

$$\frac{D^2 p'}{Dt^2} - \nabla^2 p' = \frac{D}{Dt} \left[ \delta(x) \delta(y - y_s) e^{i\omega t} \right], \quad \text{subject to} \quad -i\omega \hat{Z} \frac{d\hat{p}}{dy} = (\omega - Mk)^2 \hat{p} \quad \text{at } y = 0.$$

The detailed solution to this is given in appendix A. The result is that we may write  $p'(x, y, t; y_s) = p'_{\text{free}}(x, y, t; y_s) + p'_{\text{refl}}(x, y, t; y_s)$ , where  $p'_{\text{free}}$  is the free-field solution as if the lining were not present, and  $p'_{\text{refl}}$  is the reflected solution from the lining. The first of these is given by

$$\begin{aligned} p'_{\text{free}}(x, y, t; y_s) &= \frac{ie^{i\omega t - i\omega r(1-Mx/r)/\beta^2}}{4\pi} \int_{-\infty}^{\infty} \frac{\omega - Mk_{\text{sd}}(q)}{\sqrt{i\omega r + \beta^2 q^2/4}} e^{-q^2/2} dq \\ &= \frac{\omega \exp \left\{ i\omega \left( t + Mx/\beta^2 \right) \right\}}{4\beta^3} \left[ H_0^{(2)}(\omega r/\beta^2) - \frac{iMx}{r} H_0^{(2)'}(\omega r/\beta^2) \right], \end{aligned}$$

where  $H_0^{(2)}$  is the zeroth-order Hankel function of the second kind (see Abramowitz and Stegun<sup>31</sup>, p. 360), and

$$\begin{aligned} \beta^2 &= 1 - M^2, & r^2 &= x^2 + \beta^2(y - y_s)^2, \\ k_{\text{sd}}(q) &= \frac{\omega}{\beta^2} \left( \frac{x}{r} - M \right) - \frac{ixq^2}{2r^2} + \frac{|y - y_s|q}{r^2} \sqrt{i\omega r + \beta^2 q^2/4}. \end{aligned}$$

The reflected solution,  $p'_{\text{refl}}$ , is given by a similar integral to  $p'_{\text{free}}$ ,

$$\begin{aligned} p'_{\text{refl}}(x, y, t; y_s) &= \frac{ie^{i\omega t - i\omega \hat{r}(1-Mx/\hat{r})/\beta^2}}{4\pi} \int_{-\infty}^{\infty} \frac{\hat{\alpha}_{\text{sd}}(q)\omega \hat{Z} - (\omega - M\hat{k}_{\text{sd}}(q))^2}{\hat{\alpha}_{\text{sd}}(q)\omega \hat{Z} + (\omega - M\hat{k}_{\text{sd}}(q))^2} \frac{\omega - M\hat{k}_{\text{sd}}(q)}{\sqrt{i\omega \hat{r} + \beta^2 q^2/4}} e^{-q^2/2} dq \\ &\quad - \sum_{k \in \mathcal{K}_-} \frac{A_k(\omega - Mk)}{2\alpha} e^{i\omega t - ikx - i\alpha|y+y_s|} + \sum_{k \in \mathcal{K}_+} \frac{A_k(\omega - Mk)}{2\alpha} e^{i\omega t - ikx - i\alpha|y+y_s|} \\ &\quad - A_{k_{\text{HI}}} \frac{\omega - Mk_{\text{HI}}}{2\alpha} \exp\{i\omega t - ik_{\text{HI}}x - i\alpha|y + y_s|\}, \end{aligned} \quad (12)$$

where

$$\hat{r}^2 = x^2 + \beta^2(y + y_s)^2 \quad (13a)$$

$$\alpha(k) = \frac{-i}{\beta^2} \text{sqr}t\left(\frac{i\omega}{1-M} + ik\right) \text{sqr}t\left(\frac{i\omega}{1+M} - ik\right) \quad (13b)$$

$$\hat{k}_{\text{sd}}(q) = \frac{\omega}{\beta^2} \left( \frac{x}{\hat{r}} - M \right) - \frac{ixq^2}{2\hat{r}^2} + \frac{|y + y_s|q}{\hat{r}^2} \sqrt{i\omega \hat{r} + \beta^2 q^2/4}, \quad (13c)$$

$$\hat{\alpha}_{\text{sd}}(q) = \frac{1}{\hat{r}^2} \left[ \omega \hat{r} |y + y_s| - i\beta^2 |y + y_s| q^2/2 - xq \sqrt{i\omega \hat{r} + \beta^2 q^2/4} \right], \quad (13d)$$

and  $\text{sqrt}(\zeta) = \sqrt{\zeta}$  with  $\text{Re}(\text{sqrt}(\zeta)) > 0^a$ . The sum over  $k \in \mathcal{K}_+$  is a sum of surface modes, where  $k$  is a zero of the surface-mode dispersion relation<sup>1</sup>  $D(k, \omega) \equiv (\omega - Mk)^2 + \alpha(k)\omega\hat{Z}$  lying in the upper-half  $k$ -plane below the steepest descent contour  $\hat{k}_{\text{sd}}(q)$  for  $q \in \mathbb{R}$ . Similarly, the sum over  $k \in \mathcal{K}_-$  is a sum of surface modes where  $k$  is a zero of  $D(k, \omega)$  lying in the lower-half  $k$ -plane above the steepest descent contour. The final term of (12) is only present if a surface mode  $k_{\text{HI}}$  satisfying  $D(k_{\text{HI}}, \omega) = 0$  is to be considered an instability. The amplitudes of the surface modes are given by

$$A_k = \frac{2i(\omega - Mk)^2\alpha}{\omega\hat{Z}(\beta^2k + M\omega) + 2M(\omega - Mk)\alpha},$$

Note that while  $D(k, \omega) = 0$  is the same expression as given by Rienstra<sup>1</sup> for surface waves on an impedance surface, rather than taking  $\text{Im}(\alpha) < 0$  (as was assumed in Ref. 1 and following work<sup>2,8</sup>) we must here take the branch for  $\alpha(k)$  given by (13b) above.

### A. Incorporating a modified Myers boundary condition

If instead of the Myers boundary condition (3) we wish to use a modified Myers boundary condition, only the integrand in  $p'_{\text{refl}}$  and the pole residues  $A_k$  change. For example, if, as here, we wish to use the modified Myers boundary condition (4) for a constant-density linear boundary layer (5) of thickness  $\delta$ , then it is shown in appendix A that

$$\begin{aligned} p'_{\text{refl}}(x, y, t; y_s) &= \frac{i e^{i\omega t - i\omega\hat{r}(1-Mx/\hat{r})/\beta^2}}{4\pi} \int_{-\infty}^{\infty} \frac{(\omega\hat{Z} + iM\hat{k}_{\text{sd}}\omega\delta - 2i\hat{k}_{\text{sd}}^2M^2\delta/3)\hat{\alpha}_{\text{sd}} - (\omega - M\hat{k}_{\text{sd}})^2 - iM\hat{Z}\delta\hat{k}_{\text{sd}}^3}{(\omega\hat{Z} + iM\hat{k}_{\text{sd}}\omega\delta - 2i\hat{k}_{\text{sd}}^2M^2\delta/3)\hat{\alpha}_{\text{sd}} + (\omega - M\hat{k}_{\text{sd}})^2 + iM\hat{Z}\delta\hat{k}_{\text{sd}}^3} \\ &\quad \times \frac{\omega - M\hat{k}_{\text{sd}}}{\sqrt{i\omega\hat{r} + \beta^2q^2/4}} e^{-q^2/2} dq \\ &\quad - \sum_{k \in \mathcal{K}_-} \frac{A_k(\omega - Mk)}{2\alpha} e^{i\omega t - ikx - i\alpha|y+y_s|} + \sum_{k \in \mathcal{K}_+} \frac{A_k(\omega - Mk)}{2\alpha} e^{i\omega t - ikx - i\alpha|y+y_s|} \\ &\quad - A_{k_{\text{HI}}} \frac{\omega - Mk_{\text{HI}}}{2\alpha} \exp\{i\omega t - ik_{\text{HI}}x - i\alpha|y + y_s|\}, \end{aligned}$$

where  $\mathcal{K}_+$  and  $\mathcal{K}_-$  are the same segregation as before of solutions to the modified surface mode dispersion relation<sup>8</sup>  $D(k, \omega) = 0$  with

$$D(k, \omega) = \alpha(\omega\hat{Z} + iMk\omega\delta - 2ik^2M^2\delta/3) + (\omega - Mk)^2 + iM\hat{Z}\delta k^3,$$

and  $A_k$  are the respective surface mode amplitudes given by

$$\begin{aligned} A_k &= 2i\alpha \left( (\omega - Mk)^2 + iM\hat{Z}\delta k^3 \right) \left[ (\beta^2k + M\omega)(\omega\hat{Z} + iMk\omega\delta - 2ik^2M^2\delta/3) \right. \\ &\quad \left. + 2M(\omega - Mk)\alpha - i\alpha^2(M\omega\delta - 4kM^2\delta/3) - 3iM\hat{Z}\delta k^2\alpha \right]^{-1}. \end{aligned}$$

## V. Comparison of analytic and numerical results

As a check on both our numerical method and our analytical model, we first present results for flow over a hard wall (i.e.  $\hat{Z} \rightarrow \infty$ ) in figure 2. The agreement is seen to be excellent. Figure 2 was produced with no selective filtering, and no instabilities are observed. Moreover, figure 2 shows the entire computational domain, including buffer regions 100 points wide, and no artifacts caused by either the buffers or the domain edges can be seen. This gives confidence in both the analytic and numerical results. Note that instabilities are seen along the hard wall if the boundary condition at  $y = 0$  is implemented directly (9) rather than using the characteristics-based method described here.

For flow over an impedance lining using the Myers boundary condition, we expect to find an instability due to the illposedness of this boundary condition<sup>4</sup>. Indeed, figure 3 shows an example of the evolution of the pressure field over time which demonstrates the growth of an instability over the impedance surface. This instability dominates the acoustic waves by several orders of magnitude and would rapidly swamp the entire computational domain.

<sup>a</sup>sqrt is often the branch of the square root assumed by numerical libraries, such as `SQRT` in FORTRAN or `csqrt` in C.

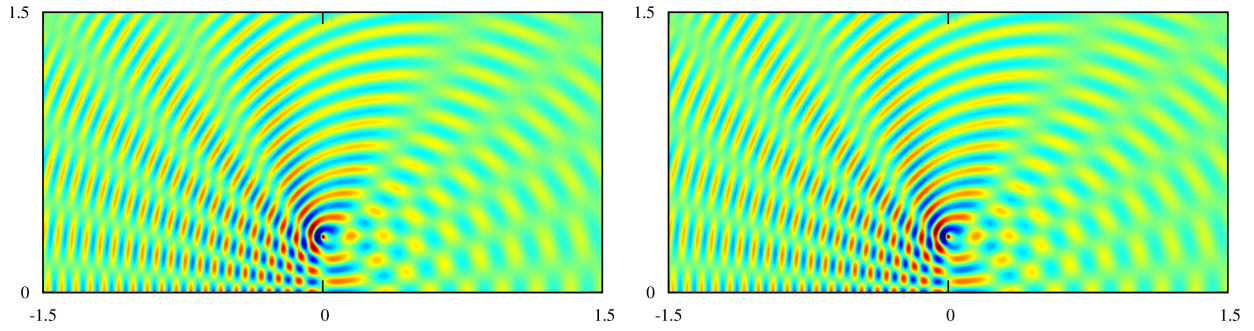


Figure 2. Comparison of pressure  $p'$  at time  $t = 32$  (after 64,000 time steps) computed numerically using §III (left) and at time  $t = \infty$  using the analytic model of §IV with the correct source phase (right), for a point source of frequency  $\omega = 16\pi \approx 50.3$  at a distance  $y_s = 0.3$  from a hard wall (modelled using the Myers boundary condition (3)) in a flow from left to right with  $u_0 = 0.4$ ,  $c_0 = 1$  and  $\rho_0 = 1$ . For the numerics, the “point” source has a Gaussian width of  $w = 2 \times 10^{-3}$ , with  $\Delta x = \Delta y = 10^{-3}$  and  $\Delta t = 5 \times 10^{-4}$  giving a CFL number of 0.7; no numerical filtering was performed. Both figures use the same colour scale.

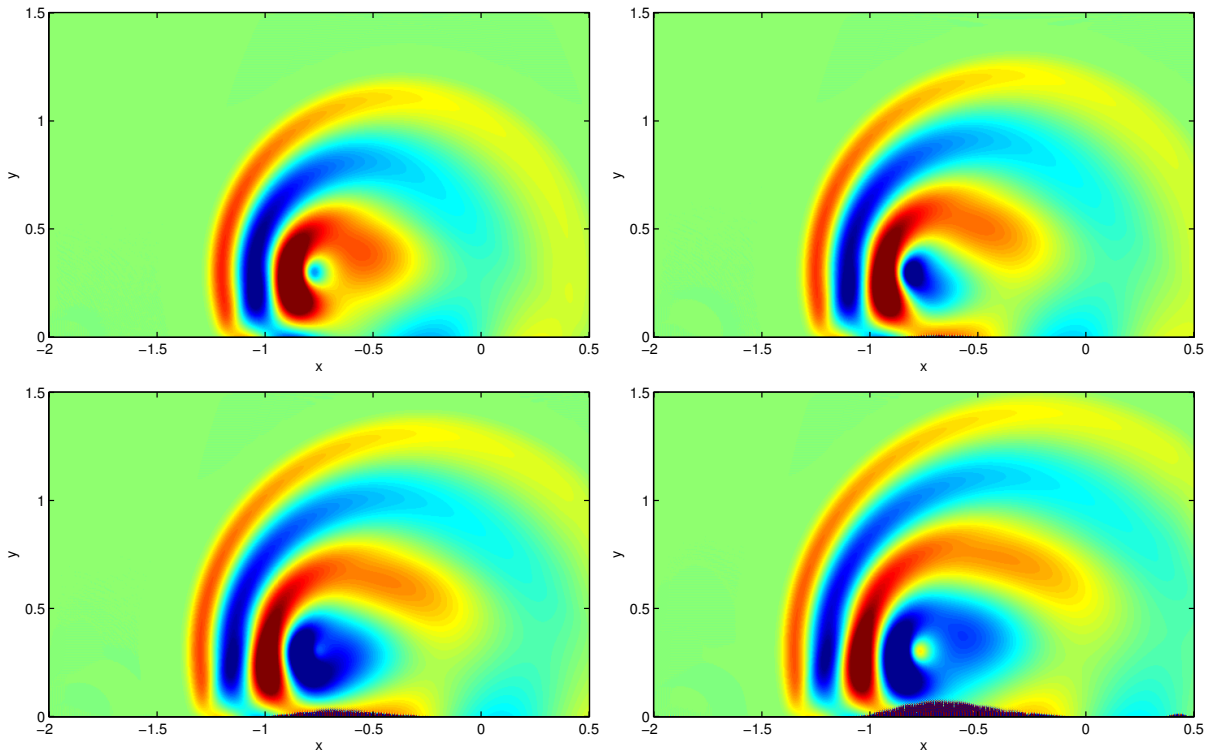


Figure 3. Snapshots of pressure in the numerical simulation using the Myers boundary condition. Note the rapid growth of an instability at the impedance surface  $y = 0$ .  $c_0 = 1$ ,  $\rho_0 = 1$ ,  $u_0 = 0.4$ ,  $\Delta x = \Delta y = 0.0035$ ,  $\Delta t = 0.002$  (so CFL = 0.8),  $\omega = 10$ ,  $(x_s, y_s) = (-0.8, 0.3)$ , a 7-point selective filtering is used, mass-spring-damper lining at  $y = 0$  with  $m = 0.08$ ,  $K = 6$ ,  $R = 1.6$ , 40 point wide buffer regions at  $x = -2$ ,  $x = 0.5$  and  $y = 1.5$ .

## VI. Dispersion analysis of the numerical model

We now present a dispersion analysis of the numerical model, so as to better understand its properties, especially the occurrence of an instability in the numerical simulation and the factors contributing to its presence. For the purpose of this analysis the computational domain is considered infinite in the  $x$  direction and we assume numerical solutions of the form  $\mathbf{q} \sim e^{-ikx}$ , which is similar to the dispersion analysis of the continuous model presented in Refs. 4,5. For the numerical model, this leads to a fully discrete eigenvalue problem, and we can study the dispersion properties of the numerical solution in terms of the angular frequency  $\omega(k)$  of each mode.

We consider a uniform grid with spacing  $\Delta x$  and  $\Delta y$ , as shown schematically in figure 4. The coordinates

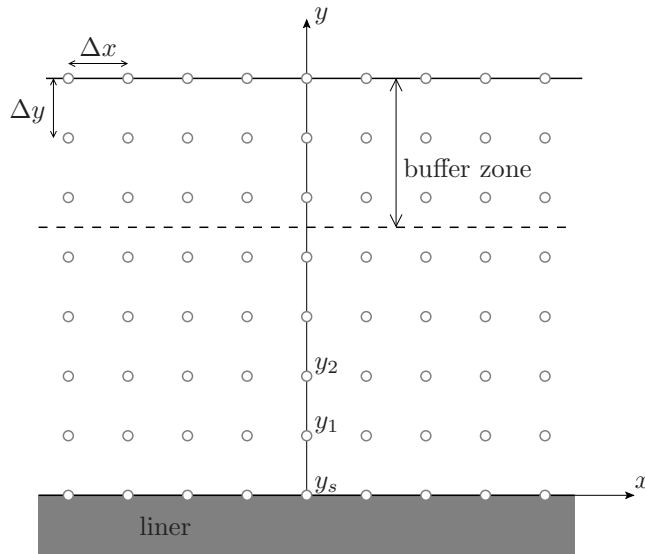


Figure 4. Diagram of the problem for the dispersion analysis of the numerical model.

of the grid points are given by  $x_m = m\Delta x$  and  $y_n = n\Delta y$ . We denote the solution at each grid point by  $\mathbf{q}_{m,n}(t)$ . With the assumed wave-like behaviour  $e^{-ikx}$ , the solution can be written

$$\mathbf{q}_{m,n}(t) = \mathbf{q}_{0,n}(t)e^{-ikm\Delta x},$$

and we are left with a finite number of degrees of freedom.

Since we are solving a linear system of equations, it is possible to write the solution at a given time step as a linear combination of the solution at the previous time step:

$$\mathbf{p}(t + \Delta t) = \mathbf{K}\mathbf{p}(t),$$

where the vector  $\mathbf{p}$  contains all the degrees of freedom, that is  $\mathbf{q}_{0,n}(t)$  together with the auxiliary variables  $\eta$  and  $\xi$  introduced for the Myers impedance condition (as well as  $\tilde{\eta}$  and  $\tilde{\xi}$  for the modified impedance condition). The coefficients in the matrix  $\mathbf{K}$  contain all the operations performed when marching the solution in time from  $t$  to  $t + \Delta t$ , including the finite-difference approximation of the flux divergence, the implementation of the impedance condition and the upper buffer zone, the time integration and the selective filter applied at each time step.

The growth rate of the solution between two time steps can be defined by the coefficient  $\lambda$  such that  $\mathbf{p}(t + \Delta t) = \lambda\mathbf{p}(t)$ . This leads to the following eigenvalue problem

$$\mathbf{K}\mathbf{z} = \lambda\mathbf{z}.$$

Alternatively we can consider the angular frequency  $\omega$  of the modes such that  $\lambda = e^{+i\omega\Delta t}$ . We obtain a set of modes, each with an angular frequency  $\omega(k)$  and eigenvector  $\mathbf{z}(k)$  parametrized by the wavenumber  $k$ . This provides a description of the dispersion properties of the numerical model. For each mode we can define the phase speed  $\omega/k$  and group velocity  $d\omega/dk$  along the  $x$  axis. In particular we are interested in unstable modes for which  $\text{Im}(\omega) < 0$  (or equivalently  $|\lambda| > 1$ ).

### A. Unstable waves: the continuous model

Before presenting results for the numerical model it is useful to review the properties of the instability in the continuous model. Figure 5 shows the typical behaviour of the growth rate of the most unstable mode, for both the continuous model with uniform flow (presented in section II) and for a boundary layer flow with a linear profile and a finite, non-zero thickness (using the same numerical method as Ref. 5). For the finite-thickness boundary layer, the growth rate initially increases with  $k$ , reaches a maximum, and then decay progressively<sup>8</sup>. The Myers boundary condition provides an approximation of the exact instability only for extremely small values of the wavenumber  $k$ . And, more importantly, the growth rate increases indefinitely with  $k$ . The fact that the growth rate remains unbounded as  $k$  increases is precisely what leads to the illposedness of the Myers condition in the time domain<sup>4</sup>.

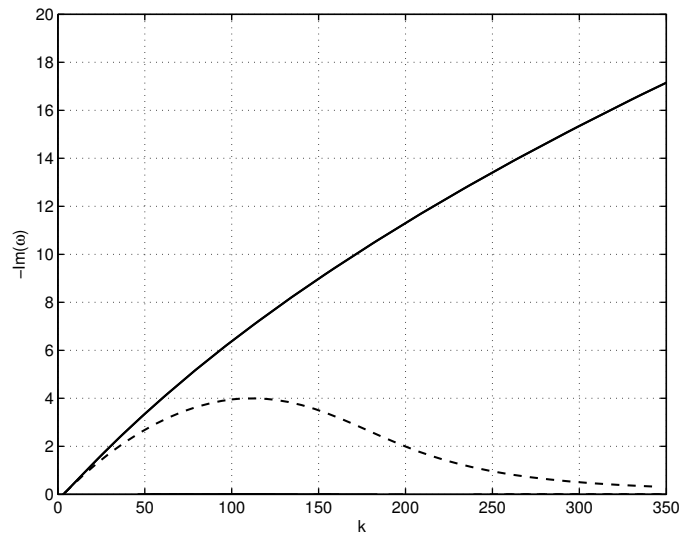


Figure 5. Growth rate of the most unstable mode as a function of the wavenumber  $k$  for the Myers condition (solid line) and for a real boundary layer with a linear profile and a thickness of  $\delta = 2 \times 10^{-3}$  (dashed line), for a flow of Mach number  $M = 0.5$  over a mass-spring-damper liner with  $m = 0.15$ ,  $K = 1.15$  and  $R = 3$ .

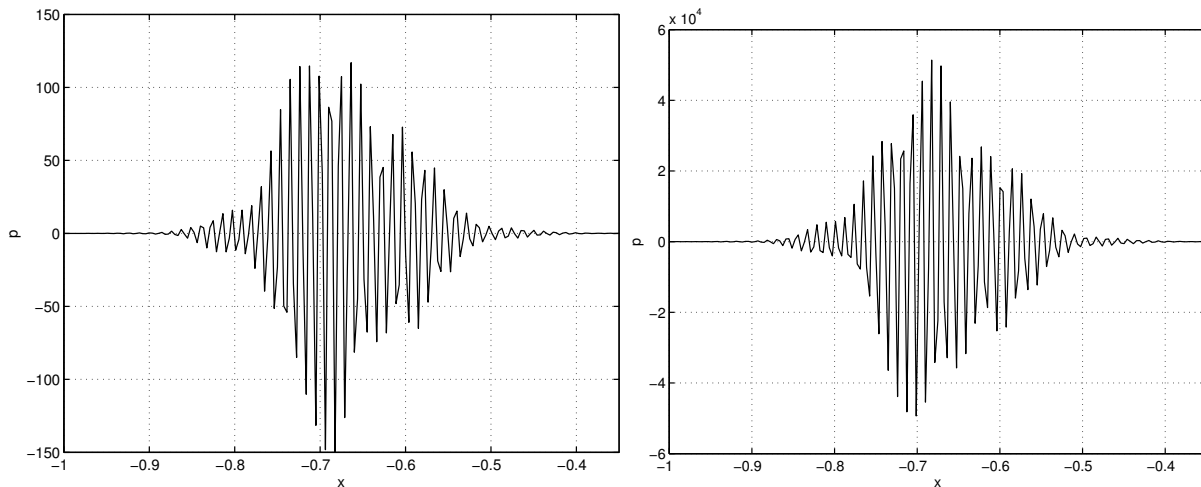


Figure 6. Instantaneous pressure  $p(x, 0, t)$  along the impedance surface at  $t = 550\Delta t$  (left) and  $t = 660\Delta t$  (right). Note the growth in amplitude between the two time steps.

## B. Unstable waves: the numerical model

We begin by showing that the instability observed in the time-domain simulation in figure 3 is correctly predicted by the dispersion analysis of the numerical model. For this purpose we compare the pressure distribution along the impedance surface  $p(x, y = 0, t)$  at two different time steps  $t_1 = 550\Delta t$  and  $t_2 = 600\Delta t$  (corresponding to the bottom left and bottom right of figure 3). As can be seen in figure 6, these take the form of a wavepacket with very short wavelength oscillations and a particularly rapid growth rate. We then calculate the spatial Fourier transforms  $\hat{p}(k, y = 0, t)$  of these solutions, shown on the left in figure 7. It is clear that these wavepackets are exclusively composed of wavenumber components between approximately  $k = 400$  and  $k = 650$ . We use the ratio between these two wavenumber spectra as an approximation of the growth rate of the individual wavenumber components that comprise the unstable wavepacket. This growth rate is compared against that predicted by the dispersion analysis on the right of figure 7, demonstrating that the growth rate predicted by the dispersion analysis matches very well with what is observed in the numerical simulation for the range of  $k$  present in the unstable wave packet. This shows that using only the most unstable mode of the dispersion analysis is sufficient to predict very accurately the instability observed in the numerical simulation.

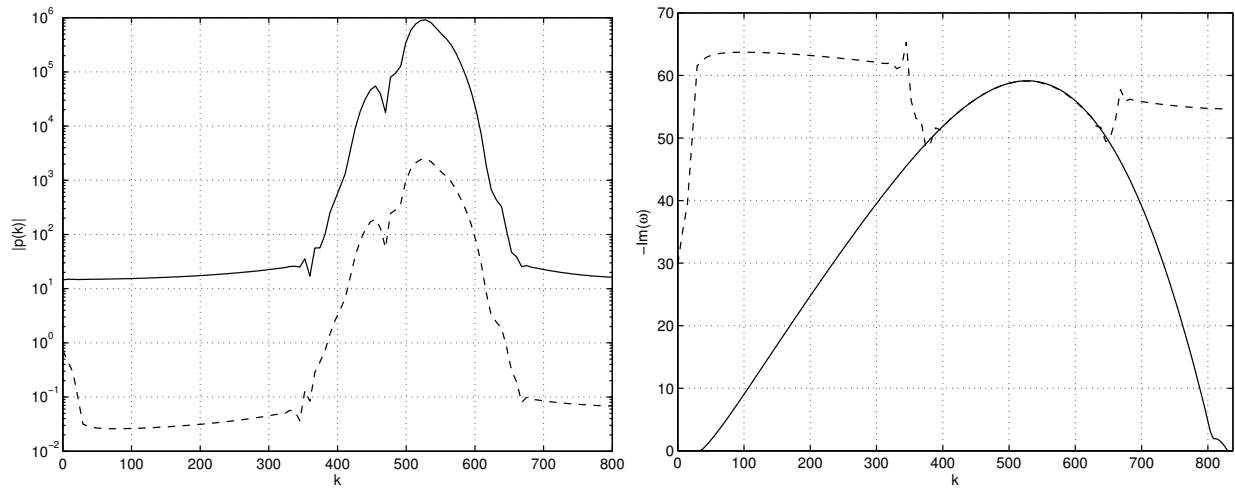


Figure 7. Left: wavenumber spectrum of the instantaneous pressure  $\hat{p}(k, 0, t)$  at  $t = 550\Delta t$  (dashed line) and  $t = 600\Delta t$  (solid line). Right: temporal growth rate of the wavenumber components predicted by the dispersion analysis (solid line) and calculated from the numerical simulation (dashed line)..

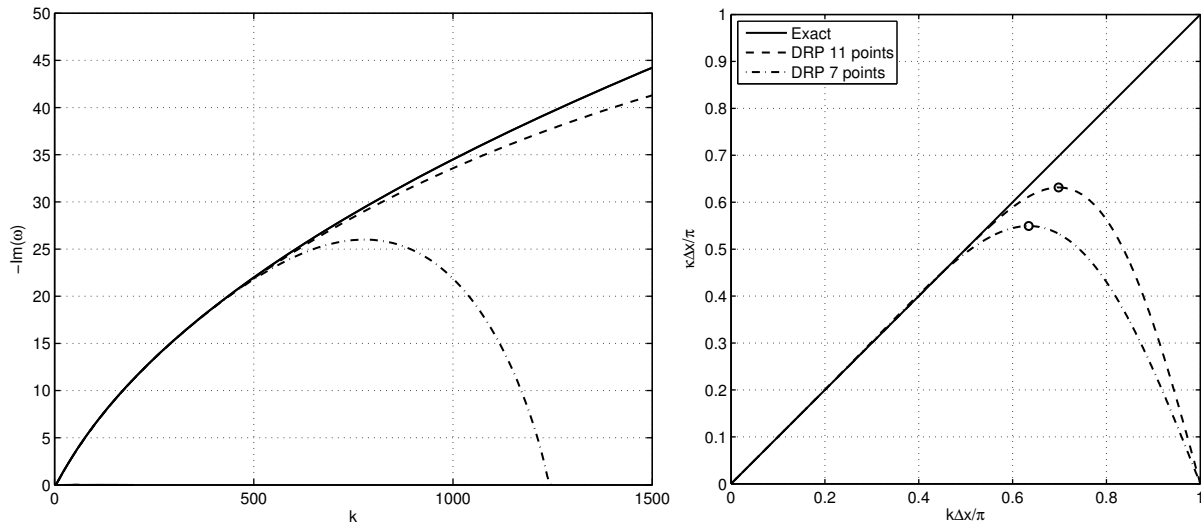


Figure 8. Left: growth rate of the most unstable mode in the numerical model as a function of the wavenumber  $k$ : continuous model (solid line); numerical model with a fine grid (dashed line); numerical model with a coarse grid (dash-dot line).

Right: dispersion properties of finite difference schemes: exact solution  $\kappa = k$  (solid line); 11-point optimized DRP scheme<sup>22,23</sup> (dashed); 7-point optimized DRP scheme<sup>21,22</sup> (dot-dashed). The symbols show the location of  $\kappa_{\max}$ .

We now consider the relation between the unstable mode of the numerical model and the instability of the continuous model. The left plot of figure 8 shows the growth rate of the most unstable mode in the numerical model as a function of the wavenumber  $k$ . Two grids, coarse and fine, are considered for the numerical model. With the fine grid the numerical mode follows the instability of the Myers boundary condition, although with a discrepancy that increases with  $k$ . This discrepancy is partly explained by the effect of the selective filtering which adds a very strong damping to large wavenumbers. The transverse pressure distribution associated with this most unstable mode is also found to match that of the continuous model. These observations indicate that the most unstable mode in the numerical model does indeed correspond to the instability of the Myers boundary condition. However, with the coarse grid the numerical solution deviates from the continuous model for  $k > 500$ , after which the numerical growth rate reaches a maximum and then starts to decrease until the mode becomes stable (i.e.  $\text{Im}(\omega) > 0$ ). This is a major difference with the continuous model based on the Myers boundary condition where the growth rate will increase indefinitely as

$k$  increases. This property of the numerical model can be explained by considering the dispersion properties of finite difference schemes. The right hand plot of figure 8 shows the normalized effective wavenumber  $\kappa\Delta x$  as a function of the true normalized wavenumber  $k\Delta x$  for two different finite difference schemes. Due to the spatial sampling of the solution, we only have to consider the range  $-\pi/\Delta x < k < \pi/\Delta x$ . As can be seen, the effective wavenumber reaches a maximum  $\kappa_{\max}$  and then decays once the wave is no longer sufficiently resolved. With finite difference schemes, and in fact most numerical approximations, the numerical model will only include effective wavenumbers bounded by  $-\kappa_{\max}$  and  $\kappa_{\max}$ , and hence large wavenumbers  $k$  behave as smaller wavenumbers  $\kappa$ . This is why in the numerical model the growth rate of the most unstable mode will not increase indefinitely with  $k$ , but instead will decrease for large wavenumbers.

This is therefore a situation where it is the inaccuracy of the finite difference scheme that renders the model more stable. And indeed as shown on the left of figure 8 the model becomes more unstable as the grid is refined. This trend is consistent with observations reported in the literature<sup>16,30</sup>.

## VII. Preliminary results for the modified Myers boundary condition

We now compare the numerical and analytic results obtained using the Myers boundary condition (3) with those obtained using the modified boundary condition (4) with a thin boundary layer of thickness  $\delta = 10^{-3}$ . Figure 9 shows one such example. On the left is the Myers boundary condition, and on the right is the modified Myers boundary condition. The top is the analytic results assuming the flow over the lining to be stable, the middle is the analytic results assuming one surface mode to be unstable (identified by Rienstra<sup>1</sup> as a possible hydrodynamic instability), and the bottom are the numerical results. Following the analysis of Refs 5 and 8, the only correct result of these six is the unstable modified one (centre right).

The modified Myers boundary condition, as implemented numerically here (figure 9, bottom right), at first sight appears significantly worse than the unmodified Myers boundary condition (figure 9, bottom left). However, figure 10 shows the growth rate of the most unstable mode of the numerics for the Myers and modified Myers boundary conditions, together with their theoretical values (for this grid spacing) for the continuous model with either uniform flow and the Myers boundary condition or a finite non-zero thickness boundary layer (using the same numerical method as Ref. 5). As can be seen, the instability of the Myers boundary condition is as described before, while the instability of the modified Myers boundary condition for  $k\Delta x/\pi < 0.8$  is approximately as it should be; it is the spurious instability at very-high wavenumbers ( $k\Delta x/\pi > 0.9$ ) that are causing the unphysical instability in this case. Such very-high wavenumbers are also not correctly modelled by the DRP scheme (see the right-hand plot of figure 8), and so there is a very valid argument for filtering out this instability. Moreover, there is an obvious separation between the real physical instability ( $k\Delta x/\pi < 0.8$  in this case) and the unphysical numerical instability ( $k\Delta x/\pi > 0.9$  in this case), so such filtering should be possible without unduly affecting the real physical instability. This is decidedly not the case with the unmodified Myers boundary condition, for which we see no such separation exists.

## VIII. Conclusions

In this paper, we investigate the numerical instability associated with the Myers boundary condition. We do this by considering the simplistic case of a 2D point mass source (or, in other words, a 3D line source) in an otherwise uniform 2D flow over an acoustic lining. The numerical scheme used has been carefully crafted to be stable without any selective filtering or damping everywhere apart from due to the impedance boundary condition (as seen from figure 2), so that any instabilities seen can be ascribed to the instability of the Myers boundary condition. These instabilities are shown to be of the type predicted by Brambley<sup>4</sup>, giving further evidence that the instability of the Myers boundary condition is due to the illposedness of the underlying mathematical formulation.

Two additional tools are used here to gain further insight into the nature of these boundary instabilities and how to control them. The first of these is the formulation of an exact analytic solution for a 2D point mass source in uniform flow over an acoustic lining, which is both used to validate the numerics in the case of a hard wall and gives benchmark solutions to compare numerical results to in the case of a lined wall. In particular, the analytic result gives the theoretical long-time harmonic solution that would be obtained if the solution were stable or if a convective (hydrodynamic) instability were present, and is able to do so both for the Myers boundary condition and for the modified Myers boundary condition of Brambley<sup>5</sup>. It is anticipated that this benchmark will prove a useful validation tool in the future, in particular to check that

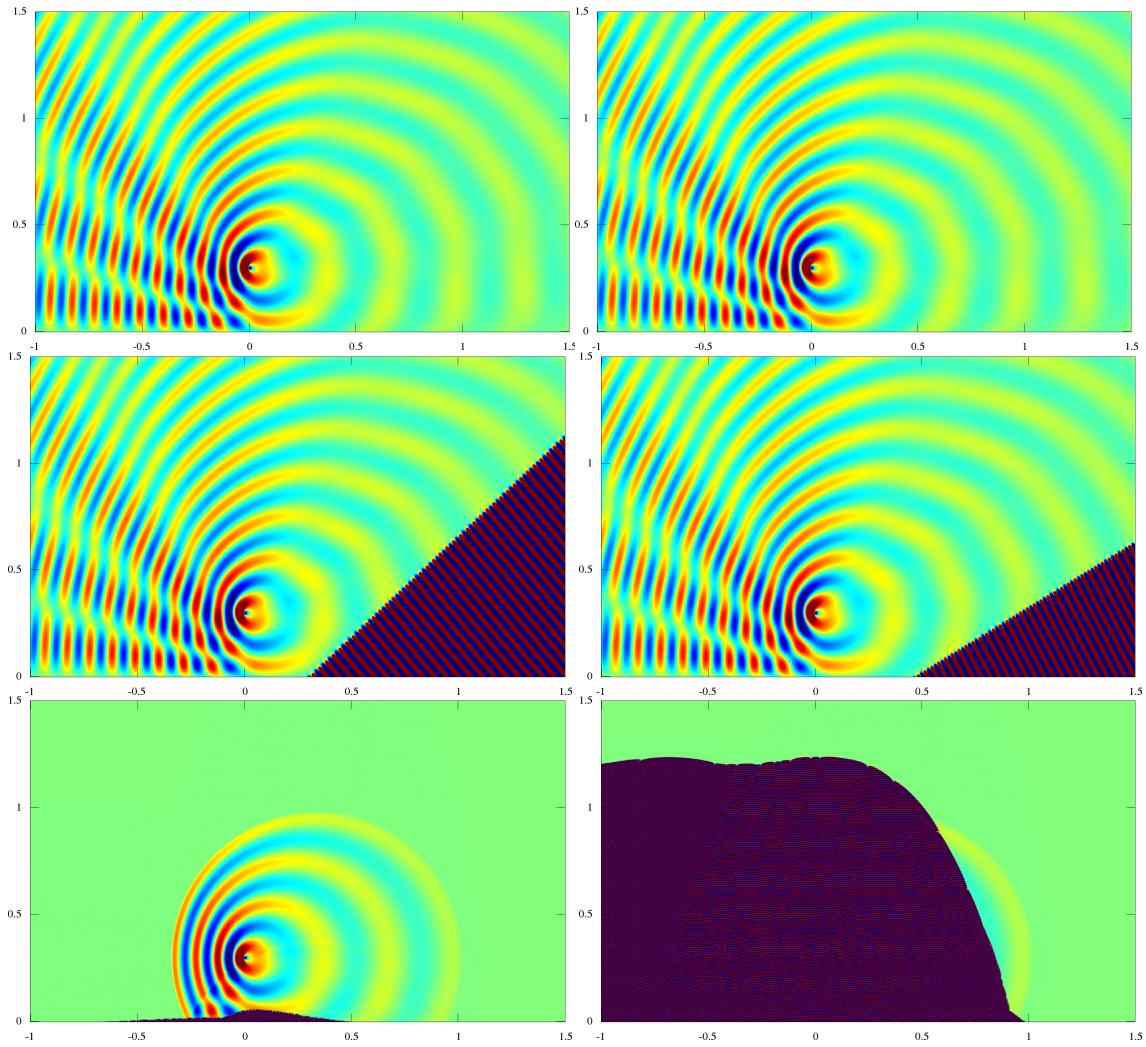


**Figure 9.** Comparison of pressure  $p'$  at time  $t = \infty$  computed using the Myers boundary condition (left) and the modified Myers boundary condition with  $\delta = 10^{-3}$  (right) using the analytic model assuming all modes to be stable (top) and the analytic model assuming an instability (middle), and the pressure  $p'$  at time  $t = 0.68$  computed numerically (bottom) using the Myers boundary condition (left) and the modified Myers boundary condition with  $\delta = 10^{-3}$  (right). The middle-right plot is the correct one.  $\omega = 31$ ,  $y_s = 0.3$ ,  $u_0 = 0.5$ ,  $c_0 = 1$ ,  $\rho_0 = 1$ ,  $w = 2 \times 10^{-3}$ ,  $\Delta x = \Delta y = 10^{-3}$ ,  $\Delta t = 5 \times 10^{-4}$  (giving CFL = 0.75),  $s = 0$ .

any numerical selective filtering is sufficiently strong for the numerics to converge to a long-time harmonic solution, but sufficiently weak to allow a convective instability when one is present.

The second tool used here is a dispersion analysis of the complete numerical model. This is shown to accurately predict the actual numerical instabilities present, and gives insight into the effect of under-resolving or over-resolving the solution for a given set of parameters. Indeed, it is this tool that allows us to identify the root cause of the instability observed in numerical simulations. It was shown here that the most unstable mode predicted by the dispersion analysis is indeed responsible for the instability observed above the liner in the time-domain simulations. It was also shown that this numerical unstable mode corresponds to the instability of the Myers condition. The main difference between the discrete and continuous model is that the growth rate of the numerical instability remains bounded while in the continuous model its growth rate increases indefinitely with the wavenumber  $k$ . This is because in the finite difference approximation the large wavenumbers that are poorly resolved behave as smaller wavenumbers, and there is therefore an upper limit  $\kappa_{\max}$  on the effective wavenumber that is represented by the numerical model.

Having positively identified the numerical instability as the theoretically-predicted one due to illposedness of the underlying mathematical problem, we then briefly consider the numerical implementation of a modified Myers boundary condition due to Brambley<sup>5</sup> designed to rectify this illposedness. At present,

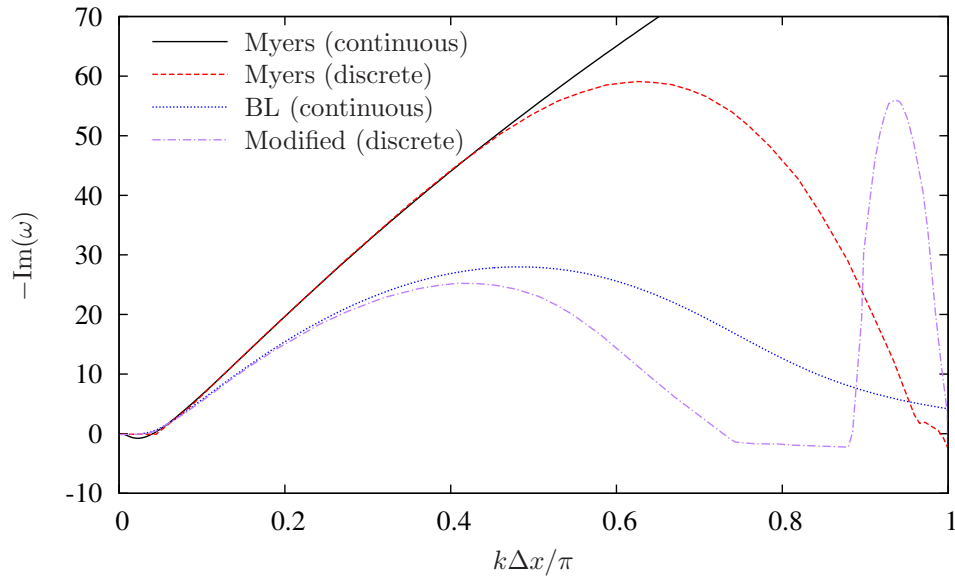


**Figure 10.** Dependence of growth rate  $-\text{Im}(\omega)$  on numerical wavenumber  $k\Delta x/\pi$  for the same parameters as figure 9 (discrete) and for the continuous model with the Myers boundary condition or with a fully-modelled linear boundary layer.

this boundary condition is shown to perform even worse than the unmodified Myers boundary condition in practice. However, through the use of our dispersion analysis, this has been shown to be due to a very-high-wavenumber instability that is an artifact inadvertently introduced to give the correct moderately-high-wavenumber behaviour. It is anticipated that a well-chosen selective filtering would be able to remove this very-high-wavenumber behaviour while still leaving the correctly-modelled moderately-high-wavenumber behaviour intact. In other words, it is anticipated that the modified Myers boundary condition used here may be implemented in such a way that a stable numerical simulation implied real-world flow stability, and an unstable numerical simulation implies real-world flow instability. This should be contrasted with the unmodified Myers boundary condition, for which no selective filtering can give the correct behaviour due to the inherent illposedness of the underlying mathematical problem. The details of how to implement the modified Myers boundary condition in practice is ongoing research.

## Acknowledgements

EJB gratefully acknowledges the support of the Royal Society for his University Research Fellowship.

### A. Details of the analytic solution

In this appendix, an analytic time-harmonic solution is found to the linearized Euler equations for uniform flow over a lining in 2D, given by (1), with a time-harmonic monopole point-forcing (2). Despite the simplicity of this situation, what follows appears to be new; Morse and Ingard<sup>28</sup> do not seem to include the solution (even without mean flow), while Junger and Feit<sup>29</sup>, p. 371 state that an analytic solution is not available in closed form for the no-flow case.

We nondimensionalize so that  $c_0 = 1$ ,  $\rho_0 = 1$ , and  $u_0 = M$  is the Mach number of the flow. Without loss of generality, we also set the  $x$ -origin such that  $x_s = 0$ . The problem to be solved in the fluid is therefore

$$\frac{D^2 p'}{Dt^2} - \nabla^2 p' = \frac{DS}{Dt}, \quad (14)$$

where the monopole source per unit distance in the  $z$ -direction is given by

$$S = \delta(x)\delta(y - y_s)e^{i\omega t}.$$

(In what follows, it is helpful to consider  $\text{Im}(\omega) = -\varepsilon$  with  $\varepsilon > 0$ , with the solution for real  $\omega$  being obtained

in the limit  $\varepsilon \rightarrow 0$ .) Fourier transforming in the  $x$ -direction and assuming a time-harmonic solution with frequency  $\omega$ ,

$$p'(x, y, t; y_s) = \frac{e^{i\omega t}}{2\pi} \int_{\mathcal{C}} \hat{p}(y; k, \omega, y_s) e^{-ikx} dk,$$

where the contour  $\mathcal{C}$  will initially be taken along the real  $k$  axis, transforms (14) into

$$\frac{d^2 \hat{p}}{dy^2} + \alpha^2 \hat{p} = -i(\omega - Mk)\delta(y - y_s),$$

where  $\alpha^2 = (\omega - Mk)^2 - k^2$  with  $\text{Im}(\alpha(k)) < 0$  for  $k \in \mathbb{R}$ . Discounting solutions which grow exponentially as  $y \rightarrow \infty$  (in effect imposing the causality argument that there is no wave inbound from infinity) gives a solution of the form

$$\hat{p} = \begin{cases} Ae^{-\alpha y} & y > y_s \\ B \sinh(\alpha y) + C \cosh(\alpha y) & y < y_s \end{cases}$$

Applying the Myers boundary condition (3),

$$-i\omega \hat{Z} \frac{d\hat{p}}{dy} = (\omega - Mk)^2 \hat{p} \quad \text{at } y = 0, \quad (15)$$

and also applying the continuity and jump of derivative conditions at  $y = y_s$ , finally gives the solution

$$p'(x, y, t; y_s) = e^{i\omega t} \int_{\mathcal{C}} \frac{(\omega - Mk)e^{-ikx}}{4\pi\alpha} \left[ e^{-i\alpha|y-y_s|} - \frac{(\omega - Mk)^2 - \alpha\omega\hat{Z}}{(\omega - Mk)^2 + \alpha\omega\hat{Z}} e^{-i\alpha(y+y_s)} \right] dk.$$

This integral may be interpreted as the sum of two terms, the first being the direct wave from the mass source  $p'_{\text{free}}(x, y, t; y_s)$  and the second being the reflection from the impedance boundary  $p'_{\text{ref}}(x, y, t; y_s)$ .

In order to simplify the numerical evaluation of  $p'_{\text{free}}$ , we deform the integration contour  $\mathcal{C}$  onto the steepest-descent contour given by  $q \in \mathbb{R}$  with

$$-ikx - i\alpha|y - y_s| = \frac{i\omega}{\beta^2}(Mx - r) - q^2/2,$$

where  $\beta^2 = 1 - M^2$  and  $r^2 = x^2 + \beta^2(y - y_s)^2$ . An example of such a contour is shown in figure 11. This gives

$$k_{\text{sd}}(q) = \frac{\omega}{\beta^2} \left( \frac{x}{r} - M \right) - \frac{ixq^2}{2r^2} + \frac{|y - y_s|q}{r^2} \sqrt{i\omega r + \beta^2 q^2/4}, \quad (16a)$$

$$\alpha_{\text{sd}}(q) = \frac{1}{r^2} \left[ \omega r |y - y_s| - i\beta^2 |y - y_s| q^2/2 - xq \sqrt{i\omega r + \beta^2 q^2/4} \right], \quad (16b)$$

with  $\text{Re}(\sqrt{\dots}) > 0$  so that the contour is traversed in the correct direction. Hence,

$$\hat{p}_{\text{free}}(x, y, t; y_s) = \frac{ie^{i\omega t - i\omega r(1 - Mx/r)/\beta^2}}{4\pi} \int_{-\infty}^{\infty} \frac{\omega - Mk_{\text{sd}}(q)}{\sqrt{i\omega r + \beta^2 q^2/4}} e^{-q^2/2} dq. \quad (17)$$

Of course, along the real- $q$ -axis a continuous branch of  $\alpha(k)$  must be chosen, as given by (16b). However, unlike the branch  $\text{Im}(\alpha(k)) < 0$  suggested for the surface mode dispersion relations of Rienstra<sup>1</sup> and Brambley and Peake<sup>2</sup>, considering  $|y - y_s| \rightarrow 0$  shows that there is only one possible branch cut of  $\alpha(k)$  that is not crossed by any steepest descent contour, shown in figure 11 as BC2. That branch is given by

$$\alpha(k) = \frac{-i}{\beta^2} \text{sqrt}(i(k + \omega/(1 - M))) \text{sqrt}(-i(k - \omega/(1 + M))) \quad (18)$$

where  $\text{sqrt}(\zeta) = \sqrt{\zeta}$  with  $\text{Re}(\text{sqrt}(\zeta)) > 0$ <sup>b</sup>. Note that this choice of branch means that  $\text{Im}(\alpha) > 0$  for some values of  $k$  (indicated by the shaded regions in figure 11).

<sup>b</sup>sqrt is often the branch of the square root that is implemented by numerical libraries, such as FORTRAN's `SQRT` or C's `csqrt` functions.

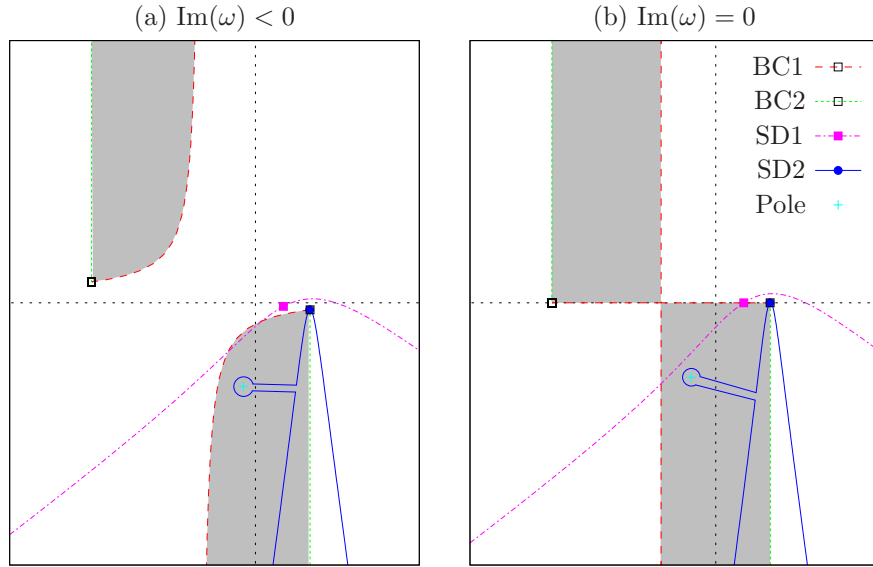


**Figure 11.** Sketch in the  $k$ -plane of the possible choices for the branch cuts of  $\alpha(k)$  and the steepest descent contours for  $p'_{\text{free}}(x, Y + y_s, t; y_s)$  and  $p'_{\text{refl}}(x, Y - y_s, t; y_s)$ . **BC1** is the branch cut for alpha given by requiring  $\text{Im}(\alpha(k)) < 0$ . **BC2** is the branch cut given by (18). The shaded region indicates where  $\text{Im}(\alpha(k)) > 0$  for branch cut **BC2**. **SD1** is the steepest descent contour for  $x/|Y| = 1$ . **SD2** is the steepest descent contour for  $x/|Y| = 10$ . Points on the steepest descent contours indicate saddle points. Poles of the integrand of (A) are also marked.

In the case of  $p'_{\text{free}}$ , the steepest descent integral (17) may be completed exactly by making the substitution

$$-q^2/2 = (i + \sinh \phi)\omega r/\beta^2, \quad q\sqrt{i\omega r + \beta^2 q^2/4} = -\cosh(\phi)\omega r/\beta,$$

and using the integral representation of the Hankel function (Ref. 31, p. 360), yielding

$$\hat{p}'_{\text{free}}(x, y, t; y_s) = \frac{\omega \exp\left\{i\omega(t + Mx/\beta^2)\right\}}{4\beta^3} \left[ H_0^{(2)}(\omega r/\beta^2) - \frac{iMx}{r} H_0^{(2)'}(\omega r/\beta^2) \right].$$

Applying the same procedure to  $p'_{\text{refl}}$  leads to

$$\begin{aligned} \hat{r}^2 &= x^2 + \beta^2(y + y_s)^2 \\ \hat{k}_{\text{sd}}(q) &= \frac{\omega}{\beta^2} \left( \frac{x}{\hat{r}} - M \right) - \frac{ixq^2}{2\hat{r}^2} + \frac{|y + y_s|q}{\hat{r}^2} \sqrt{i\omega\hat{r} + \beta^2 q^2/4}, \\ \hat{\alpha}_{\text{sd}}(q) &= \frac{1}{\hat{r}^2} \left[ \omega\hat{r}|y + y_s| - i\beta^2|y + y_s|q^2/2 - xq\sqrt{i\omega\hat{r} + \beta^2 q^2/4} \right], \end{aligned}$$

and, being careful about poles crossing the integral contour, finally to

$$\begin{aligned} p'_{\text{refl}}(x, y, t; y_s) &= \frac{ie^{i\omega t - i\omega\hat{r}(1 - Mx/\hat{r})/\beta^2}}{4\pi} \int_{-\infty}^{\infty} \frac{\hat{\alpha}_{\text{sd}}(q)\omega\hat{Z} - (\omega - M\hat{k}_{\text{sd}}(q))^2}{\hat{\alpha}_{\text{sd}}(q)\omega\hat{Z} + (\omega - M\hat{k}_{\text{sd}}(q))^2} \frac{\omega - M\hat{k}_{\text{sd}}(q)}{\sqrt{i\omega\hat{r} + \beta^2 q^2/4}} e^{-q^2/2} dq \\ &\quad - \sum_{k \in \mathcal{K}_-} \frac{A_k(\omega - Mk)}{2\alpha} e^{i\omega t - ikx - i\alpha|y + y_s|} + \sum_{k \in \mathcal{K}_+} \frac{A_k(\omega - Mk)}{2\alpha} e^{i\omega t - ikx - i\alpha|y + y_s|}, \end{aligned}$$

where

$$A_k = \frac{2i(\omega - Mk)^2\alpha}{\omega\hat{Z}(\beta^2 k + M\omega) + 2M(\omega - Mk)\alpha},$$

and  $\mathcal{K}_+$  and  $\mathcal{K}_-$  are the zeros of the dispersion relation  $D = 0$  lying either in the upper-half  $k$ -plane below the steepest descent contour (+) or in the lower-half  $k$ -plane above the steepest descent contour (-), where

$$D(k, \omega) \equiv (\omega - Mk)^2 + \alpha(k)\omega\hat{Z}.$$

Note that while  $D(k, \omega) = 0$  is the same expression as the dispersion relation for surface waves on an impedance surface<sup>1</sup>, rather than taking  $\text{Im}(\alpha) < 0$  (as was taken by Ref. 1) we must now take the branch for  $\alpha(k)$  given by (18) so that we can deform all the way onto the steepest descent contour without the branch cut getting in the way. In order to help determine whether a particular zero of  $D(k, \omega)$  should be included, it is helpful to note that setting  $x = \hat{r}(x, y) \sin(\theta)$ ,  $y + y_s = \hat{r}(x, y) \cos(\theta)/\beta$ , and  $\hat{q} = \hat{r}^{-1/2}q$  leads to

$$\hat{k}_{\text{sd}}(\hat{q}) = \frac{\omega}{\beta^2} (\sin \theta - M) - i \sin(\theta) \hat{q}^2/2 + |\cos(\theta)| \hat{q} \sqrt{i\omega + \beta^2 \hat{q}^2/4},$$

so that the steepest descent contour is a function of the observation angle  $\theta$  but is independent of the observer distance  $\hat{r}$ , and therefore particular surface modes get turned off or on at particular observation angles as the steepest descent contour crosses that particular value of  $k$ .

The above designation of zeros of the dispersion relation  $D(k, \omega) = 0$  into  $\mathcal{K}_{\pm}$  implicitly assumes that all these modes are stable evanescent modes. However, one of the zeros of the dispersion relation may be regarded as a downstream-propagating hydrodynamic instability ( $k_{\text{HI}}$ ). If this is the case, the unstable pressure  $p'_{\text{inst}}$  will differ from the pressure assuming the mode to be stable,  $p'_{\text{ref}}$  by

$$p'_{\text{inst}} - p'_{\text{ref}} = -A_{k_{\text{HI}}} \frac{\omega - Mk_{\text{HI}}}{2\alpha} \exp\{i\omega t - ik_{\text{HI}}x - i\alpha|y + y_s|\}.$$

### A. Incorporating a modified Myers boundary condition

If instead of the Myers boundary condition (15) we wish to use a modified Myers boundary condition, only the factor in  $p'_{\text{ref}}$  and the pole residues  $A_k$  change. For example, if, as here, we wish to use the modified Myers boundary condition of Brambley<sup>5</sup> for a constant-density linear boundary layer of thickness  $\delta$ , then  $\hat{Z}$  is replaced by  $\hat{Z}_{\text{eff}}$  where

$$i\omega \hat{Z}_{\text{eff}} = \frac{i\omega \hat{Z} - Mk\omega\delta + 2k^2M^2\delta/3}{1 + i\hat{Z}M\delta k^3(\omega - Mk)^{-2}},$$

and hence  $p'_{\text{ref}}$  is given by

$$\begin{aligned} p'_{\text{ref}}(x, y, t; y_s) &= \frac{i e^{i\omega t - i\omega \hat{r}(1 - Mx/\hat{r})/\beta^2}}{4\pi} \int_{-\infty}^{\infty} \frac{\alpha(\omega \hat{Z} + iMk\omega\delta - 2ik^2M^2\delta/3) - (\omega - Mk)^2 - iM\hat{Z}\delta k^3}{\alpha(\omega \hat{Z} + iMk\omega\delta - 2ik^2M^2\delta/3) + (\omega - Mk)^2 + iM\hat{Z}\delta k^3} \\ &\quad \times \frac{\omega - Mk}{\sqrt{i\omega \hat{r} + \beta^2 q^2/4}} e^{-q^2/2} dq \\ &- \sum_{k \in \mathcal{K}_-} \frac{A_k(\omega - Mk)}{2\alpha} e^{i\omega t - ikx - i\alpha|y + y_s|} + \sum_{k \in \mathcal{K}_+} \frac{A_k(\omega - Mk)}{2\alpha} e^{i\omega t - ikx - i\alpha|y + y_s|}, \end{aligned}$$

where

$$A_k = 2i\alpha \frac{(\omega - Mk)^2 + iM\hat{Z}\delta k^3}{-\alpha \partial D / \partial k},$$

and  $\mathcal{K}_+$  and  $\mathcal{K}_-$  are the same segregation as before of solutions to the dispersion relation  $D(k, \omega) = 0$ , where

$$\begin{aligned} D(k, \omega) &= \alpha(\omega \hat{Z} + iMk\omega\delta - 2ik^2M^2\delta/3) + (\omega - Mk)^2 + iM\hat{Z}\delta k^3, \\ -\alpha \partial D / \partial k &= (\beta^2 k + M\omega)(\omega \hat{Z} + iMk\omega\delta - 2ik^2M^2\delta/3) \\ &\quad + 2M(\omega - Mk)\alpha - i\alpha^2(M\omega\delta - 4kM^2\delta/3) - 3iM\hat{Z}\delta k^2\alpha. \end{aligned}$$

Note that  $D = 0$  is the same expression as the surface mode dispersion relation for the modified Myers boundary condition investigated by Brambley<sup>8</sup>, although again with a different branch cut taken for  $\alpha$ .

## References

- <sup>1</sup> S. W. Rienstra. A classification of duct modes based on surface waves. 37:119–135, 2003.
- <sup>2</sup> E. J. Brambley and N. Peake. Classification of aeroacoustically relevant surface modes in cylindrical lined ducts. 43:301–310, 2006.
- <sup>3</sup> Y. Aurégan and M. Leroux. Experimental evidence of an instability over an impedance wall in a duct with flow. *J. Sound Vib.*, 317:432–439, 2008.
- <sup>4</sup> E. J. Brambley. Fundamental problems with the model of uniform flow over acoustic linings. *J. Sound Vib.*, 322:1026–1037, 2009.
- <sup>5</sup> E. J. Brambley. A well-posed boundary condition for acoustic liners in straight ducts with flow. *AIAA J.*, 49(6):1272–1282, 2011.
- <sup>6</sup> Y. Renou and Y. Aurégan. Failure of the Ingard–Myers boundary condition for a lined duct: An experimental investigation. 130:52–60, 2011.
- <sup>7</sup> S. W. Rienstra and M. Darau. Boundary-layer thickness effects of the hydrodynamic instability along an impedance wall. 671:559–573, 2011.
- <sup>8</sup> E. J. Brambley. Surface modes in sheared boundary layers over impedance linings. *J. Sound Vib.*, 332:3750–3767, 2013.
- <sup>9</sup> M. K. Myers. On the acoustic boundary condition in the presence of flow. *J. Sound Vib.*, 71:429–434, 1980.
- <sup>10</sup> U. Ingard. Influence of fluid motion past a plane boundary on sound reflection, absorption, and transmission. 31:1035–1036, 1959.
- <sup>11</sup> W. Eversman and R. J. Beckemeyer. Transmission of sound in ducts with thin shear layers — Convergence to the uniform flow case. 52:216–220, 1972.
- <sup>12</sup> B. J. Tester. Some aspects of “sound” attenuation in lined ducts containing inviscid mean flows with boundary layers. *J. Sound Vib.*, 28:217–245, 1973.
- <sup>13</sup> W. Eversman. Approximation for thin boundary layers in the sheared flow duct transmission problem. 53:1346–1350, 1973.
- <sup>14</sup> C. K. W. Tam and L. Auriault. Time-domain impedance boundary conditions for computational aeroacoustics. *AIAA J.*, 34(5):917–923, 1996.
- <sup>15</sup> Y. Özyörük, L. N. Long, and M. G. Jones. Time-domain numerical simulation of a flow–impedance tube. *J. Comput. Phys.*, 146:29–57, 1998.
- <sup>16</sup> N. Chevaugéon, J.-F. Remacle, and X. Gallez. Discontinuous Galerkin implementation of the extended Helmholtz resonator model in the time domain. AIAA paper 2006-2569, 2006.
- <sup>17</sup> C. Richter, F. H. Thiele, X. Li, and M. Zhuang. Comparison of time-domain impedance boundary conditions for lined duct flows. *AIAA J.*, 45(6):1333–1345, 2007.
- <sup>18</sup> C. K. W. Tam, H. Ju, and E. W. Chien. Scattering of acoustic duct modes by axial liner splices. *J. Sound Vib.*, 310:1014–1035, 2008.
- <sup>19</sup> G. Gabard. A comparison of impedance boundary conditions for flow acoustics. *J. Sound Vib.*, 332:714–724, 2013.
- <sup>20</sup> S. W. Rienstra. Impedance models in time domain, including the extended Helmholtz resonator model. AIAA paper 2006-2686, 2006.
- <sup>21</sup> C. K. W. Tam and J. C. Webb. Dispersion-relation-preserving finite difference schemes for computational acoustics. *J. Comput. Phys.*, 107:262–281, 1993.
- <sup>22</sup> J. Berland, C. Bogey, O. Marsden, and C. Bailly. High-order low dispersive and low dissipative explicit schemes for multiple-scale and boundary problems. *J. Comput. Phys.*, 224:637–662, 2007.
- <sup>23</sup> C. Bogey and C. Bailly. A family of low dispersive and low dissipative explicit schemes for flow and noise computations. *J. Comput. Phys.*, 194:194–214, 2004.
- <sup>24</sup> R. L. Higdon. Initial-boundary value problems for linear hyperbolic systems. *SIAM Rev.*, 28(2):177–217, 1986.
- <sup>25</sup> J. W. Kim and D. J. Lee. Generalized characteristics boundary conditions for computational aeroacoustics. *AIAA J.*, 38(11):2040–2049, 2000.
- <sup>26</sup> S. Karni. Far-field filtering operators for suppression of reflections from artificial boundaries. *SIAM J. Num. Anal.*, 33(3):1014–1047, 1996.
- <sup>27</sup> R. D. Sandberg and N. D. Sandham. Nonreflecting zonal characteristics boundary condition for direct simulation of aerodynamic sound. *AIAA J.*, 44(2):402–405, 2006.
- <sup>28</sup> P. M. Morse and K. U. Ingard. *Theoretical Acoustics*. McGraw-Hill, 1968.
- <sup>29</sup> M. C. Junger and D. Feit. *Sound, Structures, and their Interaction*. MIT, 2nd edition, 1986.
- <sup>30</sup> H. Ju and K.-Y. Fung. Time-domain impedance boundary condition with mean flow effects. *AIAA J.*, 39(9):1683–1690, 2001.
- <sup>31</sup> M. Abramowitz and I. A. Stegun. *Handbook of Mathematical Functions*. Dover, 9th edition, 1964.